

Engineering Casimir force reduction through metallic surface nanostructuring

Francesco Intravaia,¹ Stephan Koev,^{2,3} Il Woong Jung,⁴ A. Alec Talin,² Paul S. Davids,⁵ Ricardo S. Decca,⁶ Vladimir A. Aksyuk,² Diego A. R. Dalvit,¹ Daniel López⁴

¹ Theoretical Division, MS B213, Los Alamos National Laboratory, Los Alamos, New Mexico 87545, USA

² Center for Nanoscale Science and Technology, National Institute of Standards and Technology, Gaithersburg, Maryland 20899, USA

³ Maryland Nanocenter, University of Maryland, College Park, MD 20742, USA

⁴ Center for Nanoscale Materials, Argonne National Laboratory, Argonne, Illinois 60439, USA

⁵ Applied Photonics and Microsystems, Sandia National Laboratories, Albuquerque, New Mexico 87185, USA

⁶ Department of Physics, Indiana University-Purdue University Indianapolis, Indianapolis, Indiana 46202, USA

The Casimir force is an interaction arising from quantum-mechanical fluctuations of the electromagnetic (EM) field, and is technologically significant as it results in stiction in micro- and nano-electromechanical systems (MEMS and NEMS). Control of the Casimir force has remained elusive, as many complex EM modes over a broad range of energy and length scales contribute simultaneously. Here we engineer one of two interacting gold surfaces into a high aspect ratio lamellar grating with 100 nm features, and demonstrate for the first time a strong Casimir force reduction by metallic nanostructuring. For inter-surface separations d above ≈ 400 nm, the measured Casimir force in vacuum decreases faster than the usual d^{-4} power-law reaching a value more than 2 times smaller than the one predicted by the proximity force approximation for planar-like geometries. The observed force suppression is in agreement with our ab-initio numerical analysis, and cannot be

explained by either perfect electrical conductor or effective medium descriptions. This leads us to suggest that surface plasmon-like states with evanescent EM fields may play an important role. These findings pave the way towards control and neutralization of Casimir forces for stiction mitigation in MEMS and NEMS, and highlight potential applications of plasmonics in Casimir physics.

The Casimir effect, in its most basic form, can be understood as a direct macroscopic manifestation of quantum electrodynamics, whereby changing the relative position of metallic or dielectric bodies modifies the zero point energy of the surrounding electromagnetic vacuum, resulting in a measureable interaction force between them¹. This direct connection to fundamental concepts in quantum mechanics has made this effect the object of continuous theoretical and experimental attention for over 60 years since it was first brought to light by H. Casimir. More broadly, it is also a particular case of fluctuation-induced interaction phenomena encountered in a wide variety of physical systems, such as binary liquid mixtures², cell membranes and proteins³, and even in cosmology⁴.

The Casimir force has important technological consequences and untapped application potential in the field of micro- and nano-electromechanical systems (MEMS and NEMS) – engineered devices with moveable parts ranging from 500 μm down to 10 nm in size. When the moveable parts of such devices are separated by less than 1 μm , accounting for the Casimir force can be essential for their correct design and functioning. It has been shown that this force significantly modifies both the static and the dynamic MEMS performance, leads to unwanted stiction, and is an important source of nonlinear behavior⁵. On the other hand, it has potential uses for non-contact low-dissipation actuation and tuneability of such nanomachines⁶. Beyond nanomechanics, controlling this force is important for a diversity of fields, ranging from quantum computing with atom chips⁷ to searches for non-Newtonian gravity at sub-micron scales⁸.

The seminal theoretical work of Lifshitz⁹ on the Casimir force between planar closely spaced metal and dielectric surfaces led to a complete framework for computing forces

arising from fluctuating electromagnetic fields. Well-established approximations, such as the proximity force approximation¹⁰ (PFA), have been widely utilized to extend the theory to non-planar complex geometries. The PFA assumes that the force between non-planar objects is the sum of the forces between infinitesimal planar sections computed with Lifshitz's approach. The theory has been experimentally verified under a broad range of conditions, e.g., at different length scales, where either quantum or thermal fluctuations dominate the interaction, and with different materials¹¹⁻¹⁹. However, with few exceptions^{20,21}, these precision measurements so far have been limited to planar or near-planar surfaces. The Casimir effect with complex, non-planar geometries, where simple approximations are not applicable, continues to present theoretical and experimental challenges. While the underlying theoretical principles, approaches and approximations describing the interaction of electromagnetic waves with metallic and dielectric structures of complex shapes are well established in classical photonics, the extra challenge stems from the inherently broadband nature of the Casimir effect, where fluctuations at all frequencies and wave-vectors have to be taken into account simultaneously. This not only makes the problem more complex and less amenable to an analytical solution, but also many of the abstractions based on narrow-band intuition become less applicable.

Advances in the last few years in numerical techniques give us the tools to compute the Casimir force between complex structures made of real materials^{22,23}. On the experimental side, due to the difficulties associated with the reliable fabrication of nanostructured samples and the measurement of the force, there have been very few measurements involving nanostructured surfaces. Only recently the Casimir interaction between nanostructured silicon gratings and a gold-coated sphere has been measured, with conclusive evidence of the strong geometry dependence and non-additivity of the Casimir force²⁰. Specifically, it was observed that the patterning of periodic nanoscale trenches into a silicon substrate makes the Casimir force per unit of area more *attractive* than the corresponding PFA prediction.

Metallic nanostructures have the potential to unveil a new realm for Casimir force manipulation. Indeed, they support collective surface EM modes called surface plasmons, that can propagate along the surface, decay exponentially away from it, and have a characteristic frequency of the order of the plasma frequency. In the simple plane-plane configuration, it is known that surface plasmons affect the Casimir force in a non-trivial manner, featuring an attractive (repulsive) contribution to the force for distances shorter (larger) than the plasma wavelength²⁴. A strong reduction of the Casimir force could be accomplished by engineering the geometry of the metallic structure, with the aim of substantially enhancing the repulsive plasmonic contribution. Nanostructured surfaces with tailored plasmonic dispersion relations have already impacted classical nanophotonics, with applications ranging from extraordinary light transmission to surface-enhanced Raman scattering^{25,26}. Likewise, metallic structures, with strong deviations from the planar geometry and possessing geometrical features on very small scales, are likely to give significant new insights into potential Casimir devices.

To this end we have designed and fabricated nanostructured gold gratings with critical dimensions ranging from 90 nm to 200 nm (Fig. 1A), of the order of the plasma wavelength of gold. Furthermore, we have performed high precision measurements of the Casimir force in vacuum between a gold-coated sphere and our nanostructured gold gratings. The key developments reported here are twofold: first, the ability to nanostructure metallic surfaces at nanometer scales with a precision which is at the frontier of what is now technologically possible; second, and most importantly, the capacity to control the magnitude and distance dependence of the Casimir force by tailoring the geometry of the metallic gratings.

Large area, uniform fabrication of Au nanostructures with sub-micrometer in-plane dimensions and vertical sidewalls with aspect ratio larger than one remains challenging. The standard dry etching techniques, e.g. reactive ion etching, do not generally work well for noble metals because they generate large amount of debris that re-deposit onto the structures being fabricated. Focused ion beam or ion milling may provide an alternative, but even in this case avoiding re-sputtering, creating deep vertical sidewalls and uniform

depth, and ensuring the metal on the surface is pristine is close to impossible. Techniques based on gold deposition, e.g. lift-off or sputtering, are very popular but their applicability is limited to nanostructures with small aspect ratio (<1), while achieving narrow structures with tall vertical sidewalls and uniform height is limited by the inability to uniformly fill deep trenches during deposition. We were able to achieve this by first using state-of-the-art high-voltage electron beam lithography (100 keV) to generate structures of the needed size and geometry in e-beam resist materials, and then using them as templates for pure gold deposition by either electroplating or sputtering. The e-beam parameters were carefully optimized to achieve the needed aspect ratios, separately for trenches in a positive tone resist for electroplating, and for ridges in a negative tone resist for sputtering. The gold deposition processes were also highly optimized to achieve the uniform plating thickness and the highly conformal sputtering coverage, both with low surface roughness. Figs. 1B to 1D show scanning electron microscopy (SEM) images with details of the samples used. The typical dimensions are: width w from 90 nm to 200 nm, period p from 250 nm to 800 nm, and height h from 200 nm to 500 nm. A typical sample layout is shown in Fig. 1B. As described below, the two flat uniform gold films that bound the grating area were used for system calibration and distance reference. Fig. 1C shows the uniformity of the nanofabricated surfaces and a cross-section of a single grating element is shown in Fig. 1D. See Supplementary Information for details of surface roughness and uniformity.

The experimental setup is similar to the one we have used in previous work²⁷, which allowed us to perform the most precise measurement to date of the Casimir force between metallic surfaces. Fig. 1A shows a schematic of the experimental system used (see details in Supplementary Information). It consists of a metal-coated sphere of radius $R = (151.7 \pm 0.2) \mu\text{m}$, attached to a micro-mechanical torsional oscillator. The metallic grating is attached to an optical fiber, which is used to keep the separation d between the sphere and the grating constant to within half a nanometer. As the grating is brought into close proximity of the sphere, the interaction between the two surfaces produces a shift in the oscillator resonance frequency, which can be related to the gradient of the interaction force. The apparatus was calibrated using a known interaction – the electrostatic force.

Two different calibration techniques were employed: the first one used a flat continuous film in the immediate vicinity of the grating for calibration just before performing any measurement on top of the grating area; the second one performed the whole electrostatic calibration process over the grating itself. The latter technique required calculating the sphere-grating capacitance, which was done by solving the electrostatic problem using a finite elements analysis. Both procedures produced experimentally indistinguishable results (see Supplementary Information for further details). Once the apparatus was calibrated, we extracted the gradient $\partial_d F_{sg}$ of the Casimir force between the metallic sphere and the metallic nanostructured surface. For the data analysis it is convenient to relate the sphere-grating Casimir force gradient $\partial_d F_{sg}$ with the equivalent plane-grating pressure P_{pg} . This can be done when the sphere's radius is much larger than the sphere-grating distance d , because in this situation the relevant EM field modes “see” the sphere as effectively planar. One can then approximate the sphere's surface as a collection of planar elements, and express the pressure as $P_{pg}(d) = (2\pi R)^{-1} \partial_d F_{sg}$. This is essentially a PFA treatment of the influence of the sphere's curvature in the sphere-grating Casimir force, and is an excellent approximation for the parameters of our experiment.

The finite temperature Casimir plane-grating pressure is numerically computed within the scattering formalism²³ as a series over Matsubara frequencies $\xi_l = 2\pi l k_B T / \hbar$

$$P_{pg}(d) = -k_B T \partial_d \sum_{l=0}^{\infty} ' Tr \log [I - \mathfrak{R}_p(i\xi_l) \cdot \mathfrak{N}_{pg}(d; i\xi_l) \cdot \mathfrak{R}_g(i\xi_l) \cdot \mathfrak{N}_{gp}(d; i\xi_l)]. \quad (1)$$

Here T is temperature, $\mathfrak{R}_{p(g)}$ is the reflection operator of the plane (grating), and \mathfrak{N}_{ij} are plane-wave translation operators between the two surfaces. The primed sum means that the $l=0$ term is counted with half weight. The trace operation sums over the two light polarizations, over different Brillouin zones of the periodic structure, and integrates over the parallel wavevectors k_x (direction of grating modulation) and k_y (invariant direction for grating) from $-\pi/p$ to π/p and $-\infty$ to ∞ , respectively. The broadband nature of the Casimir interaction is apparent in the above expression. The reflection operators are computed from the solution to Maxwell equations for the EM field, conveniently decomposed in terms of the natural modes of the structures²³. In our computations the

temperature is set to $T = 300$ K and we model the permittivity of gold using a Drude model $\epsilon(\omega) = 1 - \Omega_p^2 / (\omega^2 + i\Gamma\omega)$ with plasma frequency $\Omega_p = 8.9$ eV and dissipation rate $\Gamma = 0.0357$ eV (using a plasma model - $\Gamma = 0$ - produces similar numerical results for the pressure in the whole experimental range). Numerically, the errors in the computation of the Casimir pressure mainly arise from the truncation of the Matsubara sum and of the reflection and translation operators, represented as finite-size matrices. In our implementation, the total theoretical/numerical error is less than 3% over the entire pressure-displacement curve. The accuracy of our results could also be affected by the model and optical parameters chosen to describe the actual permittivity of gold used in our samples.

Fig. 2A shows the Casimir pressure between a planar gold surface and several gold nanostructured gratings with different dimensions. As expected, as the filling factor $f = w/p$ is reduced the Casimir pressure is also reduced. This is a simple effect showing the dependence of the Casimir effect on the mass density of the involved bodies: less mass implies less force. In addition, the Casimir interaction for samples with similar filling factor appears to be independent of the height of the grating. In order to clearly identify the influence of the grating geometry on the Casimir interaction, it is helpful to compare data obtained in nanostructured gratings having similar filling factors. Figures 2B and 2C show the data of two specific samples we will focus on in the remainder of the paper. Their filling factors are similar, $f_1 = 0.360$ (Fig. 2B) and $f_2 = 0.387$ (Fig. 2C). The solid lines in these figures are the result of our modal approach numerics. The good agreement between our model and the data is quantified in the insets of the same figures. The dashed lines show the behavior of the plane-grating pressure as calculated within a PFA treatment of the grating. The PFA approximates the interaction as a sum of independent local contributions from different locations. Each local pressure $P_{Lif}(x,y)$ depends on the distance between the plane and the grating surface at that location, giving as a result in this case $P_{PFA}(d) = f P_{Lif}(d) + (1 - f) P_{Lif}(d + h)$. Here $P_{Lif}(d)$ is the Casimir pressure for two parallel planes separated by a distance d , as given by the Lifshitz formula⁹. This approximation provides the same result for samples with the same f and h .

It is clear from Figs. 2B and 2C that, in our case, the PFA gives a poor description of the plane-grating Casimir pressure.

By normalizing the Casimir pressure data by the values calculated using PFA, however, one suppresses simple geometrical effects and enhances non-trivial ones. Indeed, the PFA expression takes into account the reduction of the pressure directly connected with a filling factor less than one (less matter) and with the redefinition of the distance due to the height of the grating. As is clear in Fig. 3, this normalization gives very different results even for samples with similar filling factors. At short separations ($d \leq 400$ nm) the data and the theory show an interaction per unit area more attractive compared to a flat surface (PFA), represented by the black dashed line, similarly to what has been observed in silicon gratings²⁰. However, at large separations ($d \geq 400$ nm), in metallic gratings the opposite is observed: the Casimir pressure is reduced with respect to a flat substrate. The measured pressure reaches values more than 2 times smaller than the PFA prediction. A similar behavior has been observed in all our measured metallic gratings. The separation at which the crossover between these two regimes occurs is roughly proportional to the period of the grating. This is the first experimental report of such significant pressure reduction and the crossover from enhancement to reduction.

It is worth stressing that the measured crossover is a feature of the real optical properties of our metallic gratings – in idealized perfectly reflecting gratings, PFA always underestimates the exact pressure²⁸. Furthermore, an apparent trend is clear when comparing data of nanostructures with similar filling factors but different periods: (i) at short distances, the shorter the grating period the larger the enhancement of the Casimir pressure with respect to the PFA, and (ii) at large distances, the opposite happens - shorter period leads to a stronger reduction of the Casimir force. These trends are also clearly confirmed by our numerical simulation. Since at large distances $P_{PFA}(d) \propto d^{-4}$, the data shows that the Casimir pressure decreases faster than the inverse fourth-power distance. Moreover, for fixed filling factor the rate of decrease is larger for smaller period gratings. This latter observation can be understood from a scaling argument (see Supplementary Information). At these large distances, this behavior seems to be again in

contradiction with what was predicted²⁸ and intuitively expected for ideal metals for which, in the limit of small period, one should progressively recover the plane-plane result.

In order to further look into these issues we have numerically investigated the behavior of the Casimir pressure in the large separation limit. The ratio P_{pg}/P_{PFA} shows an intriguing non-monotonic behavior, reaching a minimum and eventually going back to 1 (inset of Fig. 3). As a comparison, we also compute the plane-grating Casimir pressure in the framework of an effective medium approach²⁹. As shown in the inset, in this case P_{pg}/P_{PFA} never goes substantially below unity (see details in Supplementary Information). This leads us to suspect that the strong suppression that follows from the data at intermediate separations is probably due to non-trivial effects that go beyond a simple effective medium theory, such as complex surface bound states with evanescent EM fields³⁰. The increase of the plane-grating Casimir pressure at short separations and its reduction at larger ones with respect to the PFA, display a suggestive similarity to an enhanced contribution of surface plasmons in the plane-plane case, which are known to provide an attractive (repulsive) part to the total Casimir force at short (large) separations²⁴. However, despite the fascinating implications, these similarities require further study.

In conclusion, we have shown for the first time that the Casimir force can be dramatically reduced by using nanostructured, high-aspect ratio metallic surfaces, that set the state-of-the-art in terms of nanofabrication. The demonstrated Casimir force reduction is a substantial practical advance that is essential for MEMS and NEMS technology, as it opens new paths for reducing or eliminating unwanted adhesive forces in nano-mechanical devices. In addition to the measured force reduction, our theoretical modeling shows an intriguing distance dependency of the Casimir interaction that disagrees with standard proximity force or effective medium treatments. Surface states with evanescent electromagnetic fields supported by our plasmonic structures may be responsible for the observed novel behaviours, suggesting the potential role and impact of nanoplasmonics in Casimir physics.

1. Casimir, H. B. G. On the attraction between two perfectly conducting plates. *Proc. K. Ned. Akad. Wet.* **51**, 793 (1948).
2. Fisher, M. E. & de Gennes, P. –G. Wall phenomena in a critical binary mixture. *C.R. Acad. Sci. Paris B* **287**, 207 (1978).
3. Parsegian, V. A. *Van der Waals Forces: A Handbook for Biologists, Chemists, Engineers, and Physicist* (Cambridge University Press, Cambridge, 2006).
4. Adler, R. J., Casey, B. & Jacob, O. C. Vacuum catastrophe – An elementary exposition of the cosmological constant problem. *Am. J. Phys.* **63**, 620 (1995).
5. Chan, H. B. *et al.* Nonlinear micromechanical Casimir oscillator. *Phys. Rev. Lett.* **87**, 211801 (2001).
6. *Casimir Physics*, Lecture Notes in Physics Vol. **834**, edited by Dalvit, D.A.R., Milonni, P.W., Roberts, D.C. & Rosa, F.S.S. (Springer-Verlag, Heidelberg, 2011). Chap **9** by Decca, R. S., Aksyuk, V. A, López, D.
7. Folman, R. Material science for quantum computing with atom chips. *Quantum Inf. Process* **10**, 995 (2011).
8. Adelberger, E. G., Heckel, B. R. & Nelson, A. E. Tests of the gravitational inverse-square law. *Annu. Rev. Nucl. Part. Sci.* **53**, 77 (2003).
9. Lifshitz, E. M. The theory of molecular attractive forces between solids. *Sov. Phys. JETP* **2**, 73 (1956).
10. Derjaguin, B.V., Abrikosova, I.I. & Lifshitz, E.M. Direct measurement of molecular attraction between solids separated by a narrow gap. *Q. Rev. Chem. Soc.* **10**, 295 (1956).
11. Lamoreaux, S. K. Demonstration of the Casimir force in the 0.6 to 6 μm range. *Phys. Rev. Lett.* **78**, 5 (1997).
12. Mohideen, U. & Roy, A. Precision measurement of the Casimir force from 0.1 to 0.9 μm . *Phys. Rev. Lett.* **81**, 4549 (1998).
13. Chan, H. B. *et al.*, Quantum mechanical actuation of microelectromechanical systems by the Casimir force. *Science* **291**, 1941 (2001).
14. Bressi, G., Carugno, G., Onofrio, R. & Ruoso, G. Measurement of the Casimir force between parallel metallic surfaces. *Phys. Rev. Lett.* **88**, 041804 (2002).
15. Decca, R. S., López, D., Fischbach, E. & Krause, D. E. Measurement of the Casimir force between dissimilar metals. *Phys. Rev. Lett.* **91**, 050402 (2003).
16. Sushkov, A. O., Kim, W. J., Dalvit, D. A. R. & Lamoreaux, S. K. Observation of the thermal Casimir force. *Nat. Phys.* **7**, 230 (2011).
17. Chen, F., Mohideen, U., Klimchitskaya, G. L. & Mostepanenko, V. M. Investigation of the Casimir force between metal and semiconductor test bodies. *Phys. Rev. A* **72**, 020101(R) (2005).

18. Munday, J. N., Capasso, F. & Parsegian, V. A. Measured long-range repulsive Casimir-Lifshitz forces. *Nature* **457**, 17 (2009).
19. de Man, S., Heeck, K., Wijngaarden, R. J. & Iannuzzi, D. Halving the Casimir force with conductive oxides. *Phys. Rev. Lett.* **103**, 040402 (2009).
20. Chan, H. B. *et al.*, Measurement of the Casimir force between a gold sphere and a silicon surface with nanoscale trench arrays. *Phys. Rev. Lett.* **101**, 030401 (2008).
21. Chiu, H.-C. *et al.*, Lateral Casimir force between sinusoidally corrugated surfaces: asymmetric profiles, deviations from proximity force approximation, and comparison with exact theory. *Phys. Rev. B* **81**, 115417 (2010).
22. *Casimir Physics*, Lecture Notes in Physics Vol. 834, edited by Dalvit, D.A.R., Milonni, P.W., Roberts, D.C. & Rosa, F.S.S. (Springer-Verlag, Heidelberg, 2011). Chap. 4 by Lambrecht, A., Canaguier-Durand, A., Guérout, R. & Reynaud, S.; Chap. 5 by Rahi, S. J., Emig, T. & Jaffe, R. L.; and Chap. 6 by Johnson, S.G.
23. Davids, P.S., Intravaia, F., Rosa, F. S. S. & Dalvit, D. A. R. Modal approach to Casimir forces in periodic structures. *Phys. Rev. A* **82**, 062111 (2010).
24. Intravaia, F. & Lambrecht, A. Surface plasmon modes and the Casimir energy. *Phys. Rev. Lett.* **94**, 110404 (2005).
25. Ebbesen, T. W. *et al.* Extraordinary optical transmission through sub-wavelength hole arrays. *Nature* **391**, 667 (1998).
26. Nie, S. & Emory, S. R. Probing single molecules and single nanoparticles by surface-enhanced Raman scattering. *Science* **275**, 1102 (1997).
27. Decca, R. S. *et al.* Precise comparison of theory and new experiment for the Casimir force leads to stronger constraints on thermal quantum effects and long-range interactions. *Annals Phys.* **318**, 37 (2005).
28. Büscher, R. & Emig, T. Nonperturbative approach to Casimir interactions in periodic geometries. *Phys. Rev. A* **69**, 062101 (2004).
29. Rosa, F. S. S., Dalvit, D. A. R. & Milonni, P. W. Casimir interactions for anisotropic magnetodielectric metamaterials. *Phys. Rev. A* **78**, 032117 (2008).
30. Pendry, J. B., Martín-Moreno, L. & García-Vidal, F. J. Mimicking surface plasmons with structured surfaces. *Science* **305**, 847 (2004).

Supplementary Information is linked to the online version

Acknowledgements We are grateful to Ho Bun Chan, Peter Milonni, John Pendry, and Felipe da Rosa for discussions. This work was partially supported by the DARPA/MTO's Casimir Effect Enhancement program under DOE/NNSA Contract No. DE-AC52-06NA25396 and DOE-DARPA MIPR 09-Y557. Use of the Center for Nanoscale

Materials was supported by the U. S. Department of Energy, Office of Science, Office of Basic Energy Sciences, under Contract No. DE-AC02 06CH11357. RSD acknowledges support from the IUPUI Nanoscale Imaging Center and Integrated Nanosystems Development Institute.

Author Contributions The theoretical work was carried out by F.I., P.D., V.A.A. and D.A.R.D. The experimental work was carried out by S.K., I.W.J., A.A.T., R.S.D., V.A.A. and D.L.

Author Information Correspondence and requests for materials should be addressed to D.L. (dlopez@anl.gov).

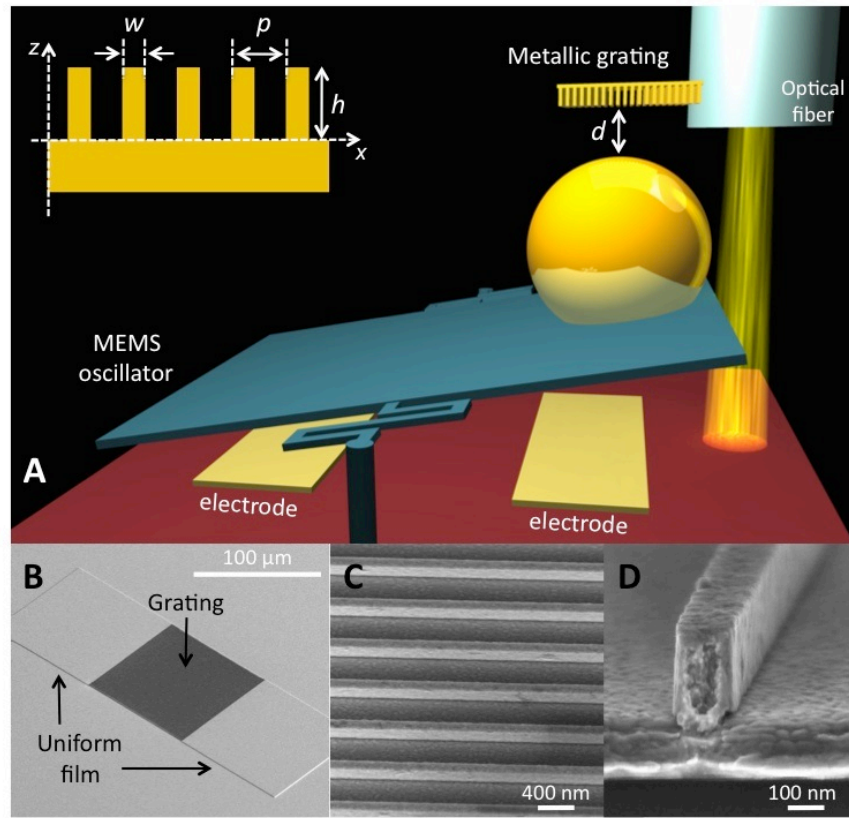


Figure 1. (A) Schematic drawing of the experimental configuration used to measure the Casimir force between a gold-coated sphere and a nanostructured grating. The sphere is attached to the torsional plate of a micromechanical oscillator and the nanostructured grating is fixed to a single mode optical fiber. The optical fiber is used to monitor the distance between the bottom of the fiber and the supporting substrate while the micromechanical oscillator provided a capacitive measurement of the Casimir interaction. (Inset) Definitions of the geometrical parameters of the metallic nanostructures. (B-D) SEM images of typical samples used in the reported experiments. (B) The nanostructured gratings are limited by two uniform films used for calibration and reference. (C) Magnified detail of the grating area showing the high spatial uniformity achieved in these samples. (D) SEM cross-sectional photograph of a single grating element.

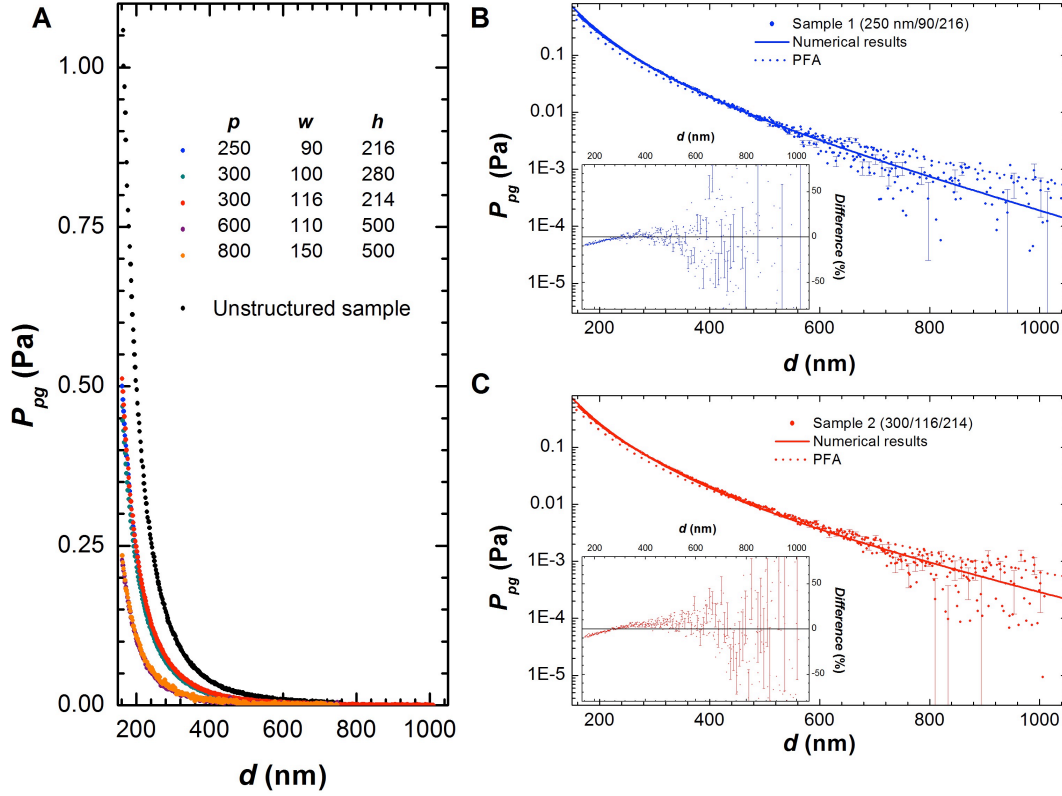


Figure 2. Equivalent plane-grating Casimir pressure P_{pg} as a function of separation between the sphere and the grating. **(A)** Measurements done for metallic nanostructured samples with different parameters. The data show that the main effect of the nanostructure is to reduce the values of the pressure according to the samples' filling factors. **(B-C)** Results for two samples of similar filling factors ($f_1 = 0.360$ and $f_2 = 0.387$, respectively): experimental measurements (dots with error bars), modal approach numerics (solid lines), and proximity force approximation (dashed lines). The insets show the relative difference between the numerical and experimental results. Error bars are the variance of the measured pressure over the 45 repetitions of the experiment for each sample. They are plotted every fifth data point to increase the clarity of the figure (see Supplementary Information for more details). Geometrical parameters of the gratings are indicated as p (period)/ w (width)/ h (height), all in nanometers.

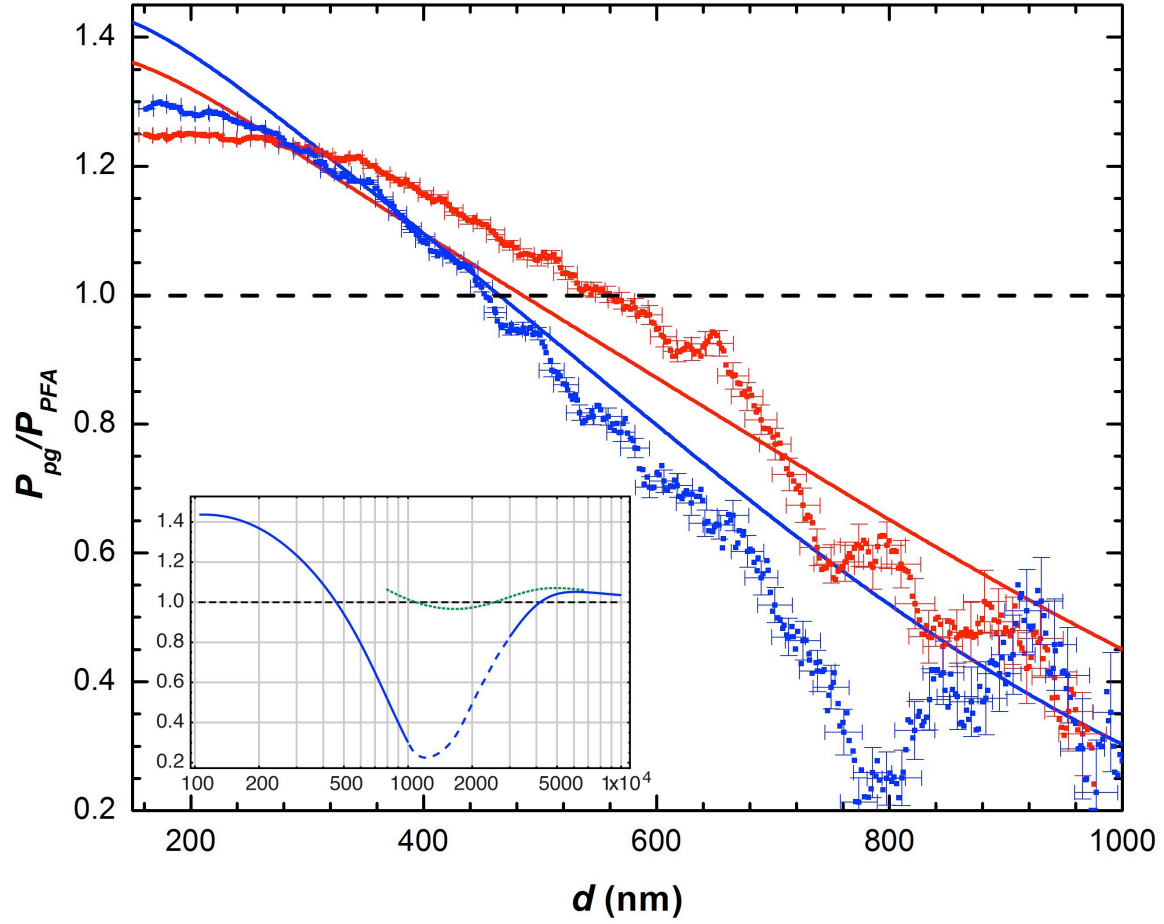
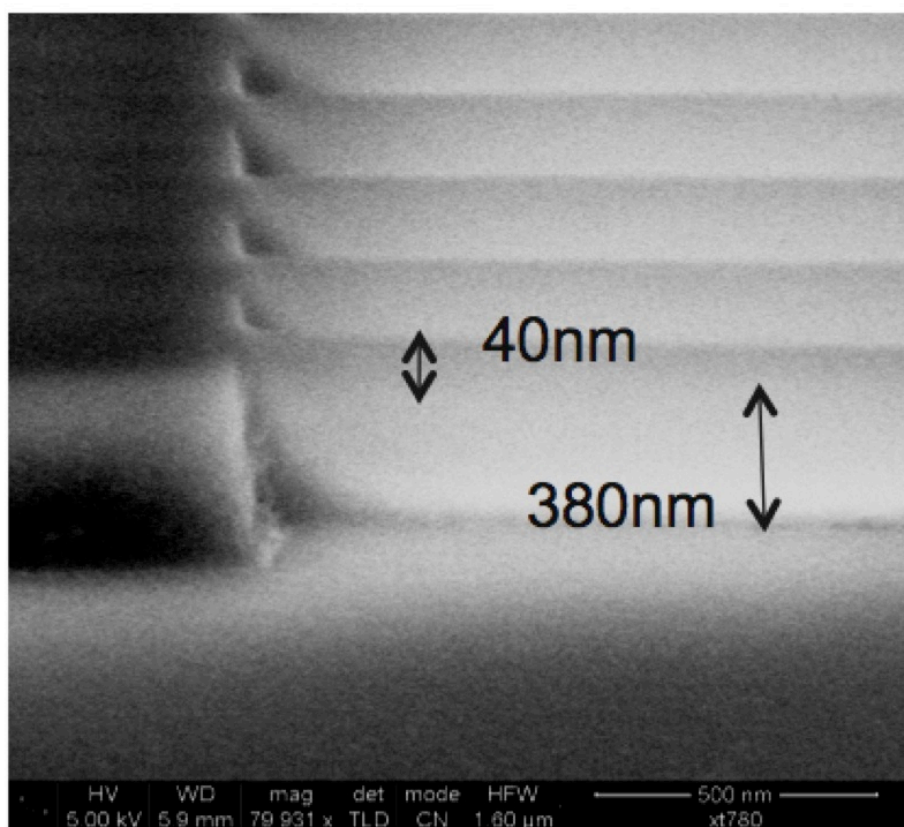


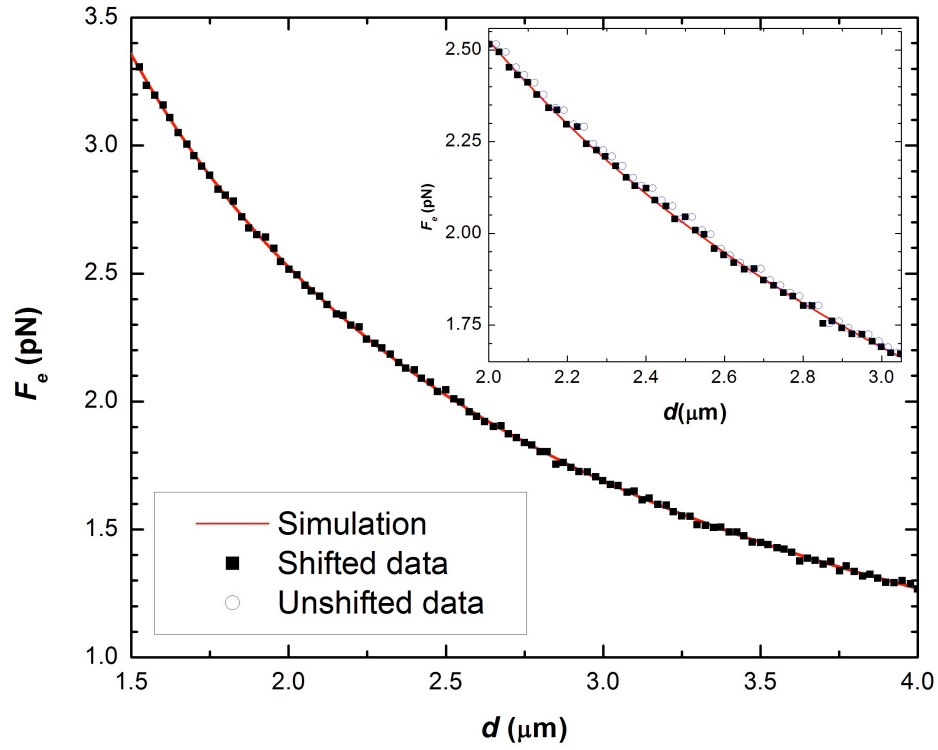
Figure 3. Effective plane-grating Casimir pressure normalized by the PFA expectations, as a function of separation between the sphere and the grating. Data are presented with dots and error bars for sample 1 (blue) and sample 2 (red). A weighted rolling average over a variable bin width is performed for the pressure, as described in the Supplementary Information, which also describes how error bars are obtained. Full lines are the modal approach numerical predictions. In the inset we plot P_{pg}/P_{PFA} for sample 1, numerically evaluated over an extended range of distances. The two solid lines give the full numerical result: at very large distances (above 3 μm) only the zeroth Matsubara term is represented since the other terms in the sum (1) can be safely neglected. Their contribution becomes, however, important in the intermediate region (between 1 and 3 μm), here sketched by the dashed curve. For comparison, the dotted (green) line represents the result of the calculation performed within an effective medium approach.

Supplementary Information

Supplementary Figures



Supplementary Figure 1. SEM image of a typical HSQ mold before deposition of Au.



Supplementary Figure 2. Plane-grating electrostatic force obtained using a commercial finite element electrostatic solver (solid lines) and the shifted measured data (black squares). The inset shows, in addition to these two sets, the data before shifting (open circles).

Supplementary Methods

Sample preparation. The nanostructured gratings used in this work were fabricated using two different methods as described below.

Method I: Sputtering of gold onto hydrogen silsesquioxane (HSQ) structures.

HSQ is an inorganic negative tone e-beam resist which is basically a spin-on dielectric with silicon dioxide-like physical properties. HSQ was patterned with an e-beam lithography system, developed and cured. In Sup. Fig. 1, we show a HSQ grating with lines having a height of 380 nm and width of 40 nm ($\approx 10:1$ aspect ratio structure).

After patterning, these HSQ structures were coated with Au by conformal sputter deposition. The conformality of our deposition is around 0.25 and hence the widening of the lines is minimal but thick enough to completely cover the dielectric with Au. After deposition of 130 nm of metal, a 40 nm wide line becomes a ≈ 100 nm wide line. This results in 4:1 aspect ratio metallic nanostructures. This method does have its limitations in the smallest width achievable due to the minimal thickness required for Au in Casimir measurements. Since HSQ itself has very smooth surfaces after patterning it results in a smooth Au surface when coated. The Au surface quality from atomic force microscopy (AFM) measurements show that the deposited Au has a RMS surface roughness of ≈ 1.0 nm and is comparable to the surface roughness of Au deposited on single crystal silicon. Varying structures with different widths (100 nm to 200 nm) and pitch (300 nm to 800 nm) were fabricated so that structures can be compared in measurements with different dimensions but similar filling factors.

Method II: Electroplating of high aspect ratio molds.

In this method the gold gratings are fabricated by electron beam lithography and electroplating. Briefly, a very high-resolution positive e-beam resist (ZEP520¹) with thickness 500 nm is spun on Si chips coated with 5 nm Ti, 200 nm Au, and 5 nm Ti layers. The resist is exposed in an e-beam lithography system at 100 kV and developed in hexyl acetate to form a high-resolution, high aspect ratio mold. The top Ti layer is then etched off in reactive ion etching, so that the Au is exposed at the bottom of the mold (the top Ti layer is necessary due to the poor adhesion of the e-beam resist to the Au surface). Next, Au electroplating is performed in an AuCN bath at room temperature using a current density of 30 A/m². The deposition rate is measured experimentally, and the time is varied to attain the desired Au thickness. After electroplating, the chip is rinsed and the e-beam resist stripped in a solvent bath. The plated structures are characterized by optical profilometry, SEM, and AFM. The measured RMS roughness of the lines is on the order of 1.5 nm, and the thickness variation across a structure is approximately 10 nm.

Experimental setup and calibration. We use a torsional oscillator (Fig. 1A) to measure the Casimir force between the gold sphere and the nanostructured gratings. The oscillator plate and a sapphire sphere are coated with a ≈ 1 nm layer of Cr followed by a ≈ 200 nm thick layer of Au. The oscillator is a $500 \times 500 \mu\text{m}^2$, $3.5 \mu\text{m}$ thick heavily doped polysilicon plate suspended at two opposite points by serpentine springs. Serpentine springs were selected over conventional torsional rods because for equal sensitivity, they occupy a smaller region and reduce vertical sag of the torsional paddle. The springs are anchored to a silicon nitride covered Si platform. When no net torque is applied, the plate is separated from the platform by a $\approx 2 \mu\text{m}$ gap. Two independently contacted polysilicon electrodes located under the plate are used to measure the capacitance (Andeen-Hagerling

¹ Disclaimer: The full description of the procedures used in this paper requires the identification of certain commercial products and their suppliers. The inclusion of such information should in no way be construed as indicating that such products or suppliers are endorsed by NIST or are recommended by NIST or that they are necessarily the best materials, instruments, software or suppliers for the purposes described.

AH2700A capacitance bridge¹) between the electrodes and the plate. The oscillator/sphere assembly is mounted on a 5-axis stepper motor driven positioner (Newport 561 series¹). The nanostructured surface is mounted on a *xyz* piezo-driven, closed-loop, 70 μm range per axis (MadCity Labs Nanopositioning System¹). Both positioning systems, which are attached to a rigid, 5 kg stainless steel structure, allow for positioning and repeatability better than 0.2 nm. The whole assembly is contained in a vacuum chamber maintained at $P = 2.6 \times 10^{-5}$ Pa. There is passive magnetic damping between the assembly and the vacuum chamber. The vacuum chamber is mounted on an optical table with active vibration isolation control (TMC Precision Electronic Positioning System¹). As measured at the sample's position, the vibrational amplitude of motion is smaller than 10 pm in the 10 Hz to 1000 Hz range. The sphere used in the experiments has a radius of curvature $R = (151.7 \pm 0.2) \mu\text{m}$. The physical parameters for the sphere (radius and sphericity) were determined by means of SEM. Both were found to be within the specifications of the manufacturer. Deposition induced asymmetries were found to be smaller than 10 nm, the resolution of the SEM. A single mode optical fiber (Corning SM-28¹) is rigidly attached to the nanostructured grating, and it is used to constantly monitor the absolute separation D between the end of the fiber and the substrate below the torsional oscillator. The RMS error in the interferometric measurements is $\delta D = 0.25$ nm, dominated by the overall stability of the closed-loop feedback system. Details on how the separation d between the sphere and a uniform sample (i.e. the pad in Fig. 1B) is obtained can be found in previous work³¹.

The apparatus is calibrated using the electrostatic interaction between the sphere and the grating/pad plate. The torsional spring constant $\kappa = (8.85 \pm 0.03)$ Nm is found in this way. Once the system is characterized a potential difference $V_o \neq 0$ between the sphere and the pad is applied to minimize, within the experimental error, the electrostatic force between the sphere and the pad. We checked that V_o is independent of position when the sphere is either on top of the pad or above the nanostructured surface.

Samples grown by metal sputtering (sample preparation method I) have equal pad and grating heights, as determined by AFM measurements. Consequently the distance D

measured between the fiber and the pad was used for obtaining the distance d between the apex of the sphere and the nanostructured surface. In contrast, in samples grown by electroplating (method II) the pad is not as high as the grating, the height difference depending on the preparation conditions. In this case, two different approaches were used: (i) The capacitance and the electrostatic force between the sphere and the grating were measured as a function of separation D . These values of electrostatic force and capacitance were compared with calculations performed using a commercial finite element electrostatic solver. It was observed that the experimental curve, when the data was plotted as a function of d (when the sphere is on top of the grating) has to be shifted by a sample-dependent amount d_o^i (≈ 15 nm) to make the calculated and measured values coincide. (ii) The height difference d_o^{ii} between the pad and the ridges was measured using an AFM. This difference was taken into account when determining the separation between the sphere and the nanostructured surface. Specifically, for the sample with $h = 400$ nm, $w = 130$ nm, $p = 350$ nm, $d_o^i = (17 \pm 2)$ nm was obtained by a least square fitting of the electrostatic force with a single fitting parameter, as shown in Sup. Fig. 2. Using the AFM method, $d_o^{ii} = (17 \pm 1)$ nm was found. In the latter case the error is the standard deviation of the values found when measuring the height difference at 25 different points. Since both methods yielded identical results within the experimental error, method (ii) was preferred due to its smaller intrinsic error.

Data reported in Fig. 3 was smoothed by performing a weighted rolling average over n consecutive points. The value of the pressure at position d is

$$\bar{P}_{pg}(\bar{d}) = \frac{\sum_{i=0}^{n-1} P_{pg}(d + i \Delta_d d) \delta P_{pg}^{-2}(d + i \Delta_d d)}{\sum_{i=0}^{n-1} \delta P_{pg}^{-2}(d + i \Delta_d d)},$$

where $\bar{d} = (1/n) \sum_{i=0}^n (d + i \Delta_d d)$, and $d + i \Delta_d d$ represent the n different separations considered. $\delta P_{pg}(d)$ is the random error in the determination of the pressure P_{pg} at distance d . The random error of the weighted rolling average is $\delta \bar{P}_{pg}(\bar{d}) = \left[\sum_{i=0}^{n-1} \delta P_{pg}^{-2}(d + i \Delta_d d) \right]^{-1/2}$. The number of data points n used in the rolling

average varies as a function of separation: $n = 10$ for $d < 300$ nm and then it increases linearly with separation to reach a value of $n = 35$ at $d = 1000$ nm, the maximum separation between the sphere and the grating. The total error in the pressure is obtained as the addition of the systematic and random errors. The maximum contribution to the systematic error $\delta \bar{P}_{pg}^{syst}$ arises from the uncertainty in the measurement of the resonant frequency ($\delta f_r = 6$ mHz) and from the error in the measurement of the sphere's radius R . The systematic error is smaller than the random error in the whole separation range. Between $300 \text{ nm} < d < 1000 \text{ nm}$, $\delta \bar{P}_{pg}^{syst} \approx 0.2 \text{ mPa}$. In the binning process, the error in the separation is determined as the variance of the different separations used, which is dominant when compared to the error in the measurement of the separation $\delta d \approx 2 \text{ nm}$.

Theoretical and numerical methods. Within the scattering approach to Casimir physics, the calculation of the plane-grating Casimir pressure is essentially reduced to the computation of the reflection operators \mathfrak{R} of the plane and the grating. For the plane \mathfrak{R}_p is given by the usual Fresnel coefficients³². For the grating \mathfrak{R}_g is computed following the modal approach²³. We divide the grating geometry into three regions (see inset of Fig. 1A): (1) the vacuum, homogeneous region $z > h$ above the grating, (2) the grating region $0 \leq z \leq h$, periodically modulated along the x -direction and invariant along the y -direction, and (3) the Au bulk, homogeneous region $z < 0$ below the grating. Within each i -th region the EM field can be expressed as a series in terms of the eigenvectors which are solutions to Maxwell equations, namely

$$F^{(i)}(x, y, z, t) = \sum_m A_m^{(i)} Y_m^{(i)}(x) e^{i\lambda_m^{(i)} z} e^{i(k_y y - \omega t)}.$$

Here F denotes any component of the electric or magnetic field, and the sum is over a discrete set of complex eigenvalues $\lambda_m^{(i)}$; the corresponding eigenvectors are denoted by $Y_m^{(i)}$. These quantities are numerically computed using an eigenvector solver. The complex coefficients $A_m^{(i)}$ are then determined by imposing boundary conditions on the vacuum-grating and grating-bulk interfaces, and finally the reflection operator \mathfrak{R}_g is obtained and employed in the Matsubara series expression for the Casimir pressure, Eq. (1).

Some analytical predictions can be made about the plane-grating pressure. First, at very large separations it is dominated by the low-frequency/low-momentum behavior of the reflection matrices: above $\approx 3 \mu\text{m}$ the zeroth Matsubara term of the sum in Eq. (1) is practically describing the whole interaction. For this term, using the Drude model for Au it is also possible to analytically solve for the eigenvalues and the eigenvectors of the EM field expansion in the grating³³. Only the transverse magnetic components matter, and in this limit the corresponding reflection matrices are equal to unity, for both the plane and the grating (the latter fact was numerically verified). Since PFA shows exactly the same behavior in the same distance range, the ratio P_{pg}/P_{PFA} must go to 1 at separations much larger than the ones accessed in the experiment (see inset of Fig. 3).

Second, in order to gain further insights into the large-separation behavior, we calculated the plane-grating Casimir pressure using an effective medium approximation³⁴ (EMA) for the nanostructure. This approximation consists in replacing the spatial-dependent electric permittivity $\epsilon(\omega, \mathbf{r})$ describing the geometrical and optical properties of the nanostructure by an effective homogeneous (not necessarily isotropic) permittivity, $\tilde{\epsilon}_{EMA}$. The EMA is expected to be valid for separations much larger than the geometrical features of the nanostructure (above $\approx 5 \mu\text{m}$). The EMA permittivity tensor is modeled as that for a uniaxial anisotropic medium²⁹, $\tilde{\epsilon}_{EMA} = \text{diag}(\epsilon_{xx}, \epsilon_{yy}, \epsilon_{zz})$ with $\epsilon_{yy} = \epsilon_{zz} = \epsilon_D f + (1 - f)$ and $\epsilon_{xx} = \epsilon_D [f + \epsilon_D(1 - f)]^{-1}$, and the resulting EMA plane-grating pressure is calculated following the technique of previous work²⁹. In the expected range of validity of EMA, the ratio P_{EMA}/P_{PFA} is always close to 1 (see inset of Fig. 3).

Third, at short ($d \leq 400 \text{ nm}$) and intermediate ($400 \text{ nm} \leq d \leq 1000 \text{ nm}$) separations, the respective enhancement and reduction of P_{pg}/P_{PFA} are stronger for the grating with the shorter period (see Fig. 3). It should be noted that the two fabricated samples have similar, but not identical, filling factors. However, it can be numerically shown that for gratings with *identical* filling factors, an analogous behavior occurs. This feature can be understood with the help of the following scaling argument. In connection with the scale

invariance of Maxwell equations, the plane-grating Casimir pressure satisfies the scaling property $P_{pg}(d, p, f, \ell) = p^{-4} P_{pg}(d/p, 1, f, \ell/p)$, where ℓ denotes all other characteristic lengths in the problem (height, Au plasma wavelength, thermal wavelength, etc.). Let us suppose that in the distance regimes considered, P_{pg} does not appreciably depend on ℓ . Then, for two gratings with identical filling factors ($f = f_1 = f_2$) but different periods ($p_1 < p_2$), the respective pressures are given by $P_1 \approx p_1^{-4} P(d_1/p_1, 1, f)$ and $P_2 \approx p_2^{-4} P(d_2/p_2, 1, f)$. One expression can be obtained from the other by using the set of linear transformations: $P_2 = (p_1/p_2)^4 P_1$ and $d_2 = (p_1/p_2) d_1$. As a direct consequence, if the pressure can be approximately described by a power-law $P \propto d^{-n}$ in a certain region of distances, then $P_1 \propto d^{-n}$ implies $P_2 \propto (p_1/p_2)^{4-n} d^{-n}$. Therefore, at the same plane-grating distance, $P_2 < P_1$ for $n < 4$ (this is the scenario in Fig. 3 at short separations) and $P_2 > P_1$ for $n > 4$ (this is the scenario in Fig. 3 at large separations). Small deviations from the above scaling argument are due to the role played by ℓ , and also to the slightly different filling factors of the two fabricated samples.

31. Decca, R. S. & López, D. Measurement of the Casimir force using a micromechanical torsional oscillator: electrostatic calibration. *Int. J. Mod. Phys. A* **24**, (2009).
32. Jackson, J. D. *Classical Electrodynamics* (Wiley, New York, 1999).
33. Li, L. A modal analysis of lamellar diffraction gratings in conical mountings. *J. Mod. Optics* **40**, 553 (1993).
34. Merlin, R. Metamaterials and the Landau-Lifshitz permeability argument: Large permittivity begets high-frequency magnetism. *Proc. Nac. Acad. Sci.* **106**, 1693 (2009).